

Numerical Viscous Flow Simulations of Cavitating Propeller Flows at Different Reynolds Numbers

Ville M. Viitanen¹, Timo Siikonen², Antonio Sánchez-Caja¹

¹VTT Technical Research Centre of Finland Ltd., Espoo, Finland.

²Department of Mechanical Engineering, Aalto University, Espoo, Finland

Abstract

In this paper, we conducted numerical simulations to investigate single and two-phase flows around marine propellers in open-water conditions at different Reynolds number regimes. Simulations were carried out using a homogeneous two-phase flow model with RANS turbulence modelling approaches. Transition was accounted for in the model-scale simulations by employing an LCTM transition model. In the model scale, also an anisotropic RANS model was utilized.

We investigated two types of marine propellers: a conventional and a tip-loaded one. We compared the results of the simulations to experimental results in terms of global propeller performance and the cavitation observations. The propeller cavitation, near-blade flow phenomena and the propeller wake flow characteristics were investigated in model- and full-scale conditions. A grid sensitivity study was carried out with respect to the propeller performance and cavitation characteristics.

The model-scale propeller performance and the cavitation patterns were captured well with the numerical simulations, with little difference between the utilized turbulence models. The global propeller performance and the cavitation patterns were similar between the model- and full-scale simulations. A tendency of increased cavitation extent was observed as the Reynolds number increases. At the same time, greater dissipation of the cavitating tip vortex was noted in the full scale conditions.

Keywords

Cavitation, CFD, Turbulence modelling, Scale effects

1. INTRODUCTION

Cavitation can cause many detrimental effects to marine propellers. It may trigger material erosion, result in vibration problems and the emission of high-intensity underwater noise. Depending on the propeller operating conditions, cavitation can appear in different forms such as a steady attached sheet cavitation on the blade surface, bubble or cloud cavitation on the blade or in the wake, and vortex cavitation at the propeller tip and hub.

Propeller global performance characteristics and boundary layer flow phenomena in non-cavitating conditions can notably vary with different Reynolds number regimes.

These aspects have been addressed, *e.g.*, by Dong *et al.* (2018); Müller *et al.* (2009); Sánchez-Caja *et al.* (2014). For instance, Rijpkema *et al.* (2015) rigorously analyzed two different marine propellers using viscous computational fluid dynamics (CFD), which operated at different Reynolds numbers in non-cavitating conditions. Baltazar *et al.* (2018) examined the $\gamma - Re_\theta$ transition model for a wetted propeller performance prediction. Sánchez-Caja *et al.* (2014) investigated the scale effects of a CLT propeller experimentally and numerically. Fig. 1 shows an example of paint tests on rough and smooth surfaces representative of full- and model-scale flow regimes. In laminar flow zones, the paint streaks on the blade surface tend to deviate from a circumferential path towards a radial direction (smooth surface) due to the lower shear stress. Conversely, the paths in the streaks corresponding to the rough surface are purely circumferential, which is indicative of turbulent flow. Typically, a distinct curve can be drawn, which separates these two flow zones, as in Fig. 1. The location of transition from laminar to turbulent flow, and the extent of the different flow zones, are quite sensitive to the Reynolds number regime in which the propeller operates. Consequently, the performance characteristics of the propeller can vary considerably (Rijpkema *et al.*, 2015). Reynolds number effects on the performance of a cavitating propeller, or on various forms of propeller cavitation structures are, however, less often reported (Amromin, 2015).

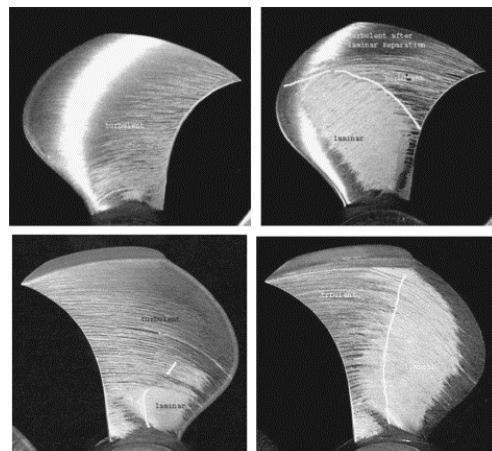


Figure 1: An example of paint test results for a CLT propeller (Sánchez-Caja *et al.*, 2014). The left frames show rough surfaces and the right frames smooth surfaces.

The aim of this paper is to investigate numerically the scale effects on propeller cavitation. Our goal is to gain deeper insight into the differences that may be found when predicting full-scale cavitation performance based on model test results. Such differences are due mainly to Reynolds number effects. In the case of conventional, non-depressurized cavitation tanks, the differences also result from the impossibility to attain cavitation number identity simultaneously at all radial stations. However, conventional facilities can use higher RPMs, guaranteeing larger Reynolds numbers, *i.e.*, turbulent flow conditions over the blades. This may avoid the use of artificial leading edge roughness usually utilized in depressurized tanks due to low the rotational speed that may be required for cavitation scaling. In this study, we simulate viscous cavitating flows in model scale as they occur in conventional tunnels. We study the model and full scale propellers in a uniform inflow condition. In reality, the fact that the propeller operates in the ship wake has some consequences in the propeller performance and cavitation, mainly resulting from the varying inflow. A complete simulation with the ship free-surface and the propeller (wetted or cavitating) is computationally intensive due to the various different time scales present.

In this paper the propeller performance is predicted numerically utilizing CFD. The range of Reynolds numbers studied covers those usually applied in the propeller open-water and cavitation tunnel model test ($Re = \mathcal{O}(10^5)$) to typical full-scale values ($Re = \mathcal{O}(10^7 \dots 10^8)$). To this end, we investigate two types of marine propellers: a conventional one, and a tip-loaded one. We employ homogeneous two-phase viscous flow modelling. Model-scale conditions are studied with three different turbulence models: the shear stress transport (SST) $k - \omega$, both with and without transition modelling, and an explicit algebraic Reynolds stress model (EARSM). The effect of transition to turbulence is investigated using the $\gamma - Re_\theta$ approach, which is coupled with the applied RANS (Reynolds averaged Navier-Stokes) model. Full-scale conditions are simulated with the SST turbulence model.

2. NUMERICAL METHOD

2.1. FLOW SOLUTION

The flow model applied is based on a homogeneous flow assumption, which is a common assumption as far as cavitation is concerned (Choi & Merkle, 1993). The governing equations for the cavitation model are

$$\begin{aligned} \frac{\partial \alpha_k \rho_k}{\partial t} + \nabla \cdot \alpha_k \rho_k \mathbf{V} &= \Gamma_k, \\ \frac{\partial \rho \mathbf{V}}{\partial t} + \nabla \cdot \rho \mathbf{V} \mathbf{V} + \nabla p &= \nabla \cdot \boldsymbol{\tau}_{ij} + \rho \mathbf{g}, \end{aligned} \quad (1)$$

where p is the pressure, \mathbf{V} the absolute velocity in a global non-rotating coordinate system, and $\boldsymbol{\tau}_{ij}$ the stress tensor, α_k is a void (volume) fraction of phase k , ρ_k the density, t the time, Γ_k the mass-transfer term, and \mathbf{g} the gravity vector. The void fraction is defined as $\alpha_k = \mathcal{V}_k / \mathcal{V}$, where

\mathcal{V}_k denotes the volume occupied by phase k of the total volume, \mathcal{V} . For the mass transfer $\sum_k \Gamma_k = 0$ holds, and consequently only a single mass-transfer term is needed.

A compressible form of the flow equations is solved. Although the phase temperatures do not play a significant role in cavitation, the energy equations (not shown here) must be present in order to predict the correct acoustic signal speeds. The phase temperatures also have some influence on the solution via the gas density and the viscosities. For the mixture momentum equation, the density and the viscosity are evaluated from

$$\rho = \sum_k \alpha_k \rho_k \quad \text{and} \quad \mu = \sum_k \alpha_k \mu_k, \quad (2)$$

where μ is the dynamic viscosity. The turbulence effects are currently handled using single-phase models for the mixture.

The finite volume method is utilized to discretize the governing equations. For the time derivatives, a second-order three-level fully implicit method is used. The viscous fluxes as well as the pressure terms are centrally differenced. For the convective part, the variables on the cell surfaces are evaluated using a third-order upwind-biased MUSCL (monotonic upstream-centred scheme for conservation laws) interpolation (Van Leer, 1982). A flux limiter can be applied, but in this study this is done only for the void fraction. The application of a limiter function to the convective fluxes of the void fraction may be necessary, since it is essentially a discontinuous quantity through the phase boundary. This may lead to problems in a numerical solution, and the void fraction could locally obtain non-physical values amidst an iterative solver. Additionally, cavitation volumes can exhibit rapid temporal and spatial variation when, for instance, bursts of cloud cavities or fine cavitating vortices are present. Previously, it was shown that a compressive limiter with the void fraction equation especially improves the predicted tip vortex cavitation patterns (Viitanen & Siikonen, 2017). Hence, a compressive ‘‘superbee’’ limiter of Roe (1985) is employed for the cavitating cases considered in this study as well.

2.2. MASS AND ENERGY TRANSFER

In this study, the mass-transfer model is similar to that of Choi & Merkle (1993):

$$\begin{aligned} \Gamma_l &= \frac{\rho_l \alpha_l \min [0, p - p_{\text{sat}}]}{\frac{1}{2} \rho_\infty V_\infty^2 (L_{\text{cav}} / V_{\text{cav}}) \tau_l} \\ &+ \frac{\rho_g \alpha_g \max [0, p - p_{\text{sat}}]}{\frac{1}{2} \rho_\infty V_\infty^2 (L_{\text{cav}} / V_{\text{cav}}) \tau_g}, \end{aligned} \quad (3)$$

where p_{sat} is the saturation pressure, ρ_∞ the reference (inlet) density, and V_∞ the corresponding velocity. The evaporation time constants were made non-dimensional using the reference length L_{cav} and the velocity related to cavitation (V_{cav}). In some cases, such as on a propeller blade, the cavitation length and velocity differ from the reference length L_{ref} and the reference velocity (V_∞). The time constants correspond to the parameters of the original model as

$\tau_l = 1/C_{\text{dest}}$ and $\tau_g = 1/C_{\text{prod}}$. The empirical parameters of the cavitation model are calibrated in (Sipilä, 2012).

In the present study, the saturation pressure was based on the given free-stream temperature, and the gas phase was assumed to be saturated (i.e., $T_g = T_{\text{sat}}$). Since the gas temperature was forced to be $T_g = T_{\text{sat}}$, $q_{ig} = 0$. From the interfacial energy balance, the interfacial heat transfer can be solved for the liquid phase

$$q_{il} = -(h_{g\text{sat}} - h_{l\text{sat}})\Gamma_g - q_{ig} = (h_{g\text{sat}} - h_{l\text{sat}})\Gamma_l. \quad (4)$$

Using Equations (3) and (4), the interfacial transfer terms in the continuity and energy equations are obtained.

2.3. TURBULENCE MODELLING

The base turbulence model applied in the present calculations is the SST $k - \omega$ of Menter (1992). The SST $k - \omega$ is a zonal model, referring to the formulation where the $k - \omega$ equations are solved only inside the boundary layer, and the standard $k - \varepsilon$ equations, transformed to the ω -formulation, are solved away from the walls. In model scale, the SST model was used also in connection with the EARSM of Wallin & Johansson (2001), as well as the $\gamma - Re_\theta$ transition model. The calculations were performed up to the wall both in the model- and full-scale simulations. The non-dimensional wall distance was adjusted such that $y^+ \approx 1$ for the first cell. The turbulence modelling was applied for the mixture.

The effect of transition was investigated using the $\gamma - Re_\theta$ approach in model scale. In the $\gamma - Re_\theta$ transition model (also known as a Local Correlation-Based Transition Model LCTM) two extra field equations are inserted for turbulence modelling (Langtry, 2006; Langtry *et al.*, 2006; Menter *et al.*, 2006). The purpose of the transport equation for turbulence intermittency γ , is to produce variable γ , which is coupled with the SST turbulence model to trigger transition in the boundary layer:

$$\begin{aligned} \frac{\partial(\rho\gamma)}{\partial t} + \frac{\partial(\rho u_j \gamma)}{\partial x_j} \\ = P_\gamma + \frac{\partial}{\partial x_j} \left[\left(\mu + \frac{\mu_t}{\sigma_f} \right) \frac{\partial \gamma}{\partial x_j} \right]. \end{aligned} \quad (5)$$

Here P_γ is the contribution from all of the source and destruction terms and σ_f is a Schmidt number. The transport equation for the *local* transition onset momentum thickness Reynolds number $\widetilde{Re}_{\theta t}$ captures the non-local effects of the free-stream turbulence intensity into the boundary layer:

$$\begin{aligned} \frac{\partial(\rho \widetilde{Re}_{\theta t})}{\partial t} + \frac{\partial(\rho u_j \widetilde{Re}_{\theta t})}{\partial x_j} \\ = P_{\theta t} + \frac{\partial}{\partial x_j} \left[\sigma_{\theta t} (\mu + \mu_t) \frac{\partial \widetilde{Re}_{\theta t}}{\partial x_j} \right]. \end{aligned} \quad (6)$$

The SST $k - \omega$ is an isotropic turbulence model, i.e., it predicts the Reynolds stress tensor according to the Boussinesq approximation. In other words, no individual modelling is employed for each normal turbulent stresses; only

their sum, $k = \overline{u'_i u'_i} / 2$, is modelled. To account for turbulence anisotropy, the EARSM can be utilized. The idea in algebraic Reynolds stress models is to allow a non-linear relationship between the rate of mean strain and the Reynolds stresses, but without the need of solving additional partial differential equations for each of the six Reynolds stresses. The EARSM relies on the two-equation formulation but with the Reynolds stress anisotropy tensor evaluated from a linear pressure-strain model, and forms a physically well-founded strategy among two-equation models for improved prediction of flows involving complex features such as streamline curvature effects and system rotation (Hellsten, 2002; Hellsten *et al.*, 2002).

2.4. SOLUTION ALGORITHM

The solution method is a segregated pressure-based algorithm where the momentum equations are solved first, and then a pressure-velocity correction is made. The basic idea in the solution of all equations is that the mass balance is not forced at every iteration cycle, but rather the effect of the mass error is subtracted from the linearized conservation equations. A pressure correction equation was derived from the continuity Equation (1) linked with the linearized momentum equation.

In order to decrease the oscillations in the solution owing to the rapid changes in the mass transfer, the mass-transfer rate was under-relaxed between the iteration cycles as $\Gamma_l^{n+1} = \alpha_\Gamma \Gamma_l^* + (1 - \alpha_\Gamma) \Gamma_l^n$, where $\alpha_\Gamma = 0.5$ is an under-relaxation factor, n refers to the iteration cycle, and Γ_l^* is calculated from Equation (3). For small values $|\Gamma_l^n| < 0.1$ (kg/m³s), under-relaxation was not applied.

In the pressure-correction equation the mass-transfer term is pseudo-linearized in order to increase stability. The velocity-pressure coupling is based on the corresponding algorithm for a single-phase flow (Miettinen & Siikonen, 2015), and is described in more detail by Viitanen & Siikonen (2017).

The flow equations are solved using a quasi-steady approach. Absolute velocities were used in the solution, and the rotational movement of the propeller was accounted for in the convection velocity and as source terms in the y - and z -momentum equations as the propeller rotates about the x -axis. The equations were iterated until the global force coefficients and the L_2 norms of the main variables obtained a sufficiently steady level, with the L_2 norms having decreased to $10^{-5} \dots 10^{-7}$.

3. TEST CASES

Two propellers are considered in this study: the PPTC (Potsdam propeller test case) propeller (Heinke, 2011) and a TLP (tip loaded propeller) propeller. The former is a more conventional five-bladed propeller with moderate skew, while the latter is a pressure-side oriented tip blade propeller with enhanced efficiency.

Photographs of the propellers are shown in Fig. 2. The

principal data of the studied propellers is given in Tab. 1 for the PPTC and in Tab. 2 for the TLP.

Table 1: Main geometric parameters of the PPTC propeller (Heinke, 2011).

Diameter [m]	0.250
Pitch ratio at $r/R = 0.7$	1.635
Chord at $r/R = 0.7$	0.417
EAR	0.779
Skew [$^\circ$]	18.837
Hub ratio	0.300
Number of blades	5
Rotation	Right handed

Table 2: Main geometric parameters of the TLP propeller.

Diameter [m]	0.250
Pitch ratio at $r/R = 0.7$	1.465
EAR	0.594
Number of blades	5
Rotation	Right handed

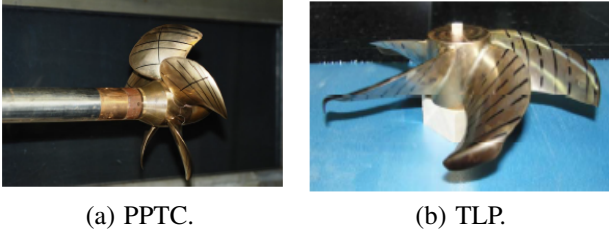


Figure 2: Photographs of the investigated propellers.

The advance coefficient and cavitation number are defined as

$$J = \frac{V_A}{nD} \quad \text{and} \quad \sigma_n = \frac{p - p_{\text{sat}}}{\frac{1}{2}\rho(nD)^2}, \quad (7)$$

respectively, where V_A is the propeller speed of advance, n the propeller rate of revolutions and D the propeller diameter, p is the pressure, p_{sat} the saturation pressure and ρ the fluid density. The thrust and torque of the propeller are non-dimensionalized as

$$K_T = \frac{T}{\rho n^2 D^4} \quad \text{and} \quad K_Q = \frac{Q}{\rho n^2 D^5}, \quad (8)$$

respectively, where T denotes the thrust and Q the torque of the propeller. The Reynolds number is defined as

$$Re = \frac{\rho c_{0.7} \sqrt{V_A^2 + (0.7\omega D/2)^2}}{\mu}, \quad (9)$$

where $\omega = 2\pi n$, and $c_{0.7}$ denotes the chord length at $r/R = 0.7$ radius. The investigated conditions for the cavitating cases are listed in Tab. 3 for each propeller. We study the cases at two different Reynolds numbers.

In the following, the cases are referred to as model-scale ($Re = 1.3 \times 10^6$ for the PPTC, and $Re = 9.7 \times 10^5$ for the TLP) and full-scale ($Re = 2.9 \times 10^7$ for the PPTC, and $Re = 5.7 \times 10^7$ for the TLP) conditions. The model-scale conditions were chosen to match the experimental conditions, and the full-scale conditions were selected to ensure a sufficiently high Reynolds number. The reference length and velocity scales related to the Merkle cavitation model, discussed in 2.2, were here the chord and the speed at $r/R = 0.7$ radius. We used the same values for the empirical parameters in the cavitation model in model and full scale simulations, and they were $C_{\text{dest}} = C_{\text{prod}} = 369$.

Table 3: Test conditions for the cavitating cases.

Quantity	PPTC	TLP
J	1.019	0.729
σ_n	2.024	4.092
K_T	0.374	0.493
n [rps]	25.0	15.0

3.1. COMPUTATIONAL SETUP

Two grids were constructed for both propellers: a model scale grid and a full scale grid. The model scale grids were generated to simulate the experimental setups. The computational grids for the full scale simulations were scaled from the model scale grids, and additional cells were clustered close to solid surfaces to ensure that $y^+ \approx 1$ for the simulations. The scaling factor for PPTC was 12, and for the TLP this was 26.

The computational domain is shown in Fig. 3 for the PPTC propeller. Corresponding design for the computational domain was used for TLP propeller. The calculations were performed with three grid densities. On the coarse grid level, every second point in all directions is removed compared to the finer level grid. A solution on the coarse grid is used as an initial guess for the computations performed on the next finer grid level. The fine computational grid used for the PPTC propeller consists of roughly 6.5 million cells in 36 grid blocks, the medium grid consists of 0.8 million cells, and the coarse grid of 0.1 million cells. The fine grid for the TLP consists of roughly 10 million cells in 45 grid blocks, the medium grid consists of 1.3 million cells, and the coarse grid of 0.2 million cells. The different grids on the suction sides of the propeller blades are shown in Fig. 4. The surface grid on the pressure sides of the blades is similar. A similar grid for the PPTC was used before (Viitanen & Siikonen, 2017; Viitanen *et al.*, 2018), but the grid density in the wake region was increased for this study. Due to the symmetric nature of the problem of a propeller operating in uniform inflow, only one blade is modelled. The blades, hub and shaft are modelled as no-slip rotational surfaces. A velocity boundary condition is applied at the inlet and a pressure boundary condition is applied at the outlet. A slip boundary condition is applied at the simplified cavitation tunnel walls.

The whole computational domains are considered as ro-

tating with the given rate of rotation. The inflow velocity is set based on the advance numbers of the propeller, and the background pressure level is set based on the cavitation number. Low turbulent intensity and eddy viscosity ratio, $< 1\%$, were used as initial conditions in all calculations. The inlet is located roughly five propeller diameters upstream of the propeller, and the outlet is located ten diameters downstream of the propeller. For the PPTC propeller, the radius of the whole computational domain is 0.3385 m in model scale, which corresponds to the cross-sectional area of the experimental cavitation tunnel. The radius of 0.7 m in model scale was used for the computational domain for the TLP, which was larger in cross-sectional area than in the experimental tank.

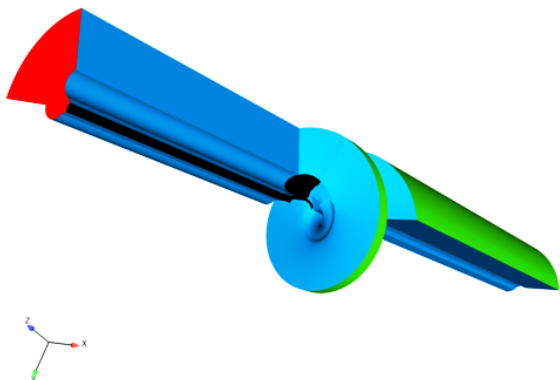


Figure 3: Perspective view of the computational domain utilized in the calculations for the PPTC propeller. The propeller, hub and shaft are coloured with black. The inlet face is coloured with red. The cyclic boundaries are coloured with blue, and the simplified tunnel wall is coloured with green.

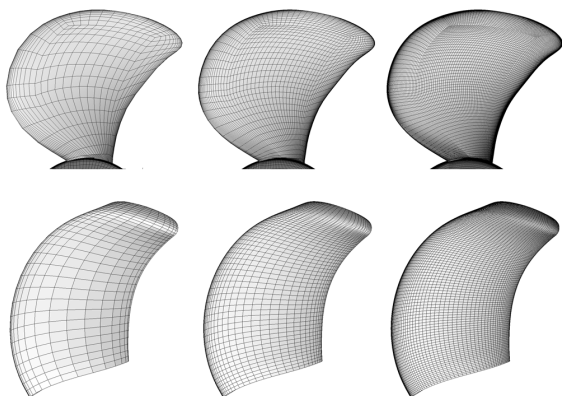


Figure 4: Grid density on the suction sides of the PPTC (top row) and TLP (bottom row) propeller blades. Coarse (left), medium (middle), and fine (right) model-scale grids shown.

4. RESULTS

This section is organized as follows. We first compare the numerical simulations to experimental values in terms of the open-water characteristics, in Sec. 4.1.1, and the

model-scale cavitation observations in Sec. 4.1.2. A grid dependency investigation is carried out in Sec. 4.1.3. Next, we compare the observed propeller cavitation phenomena with the different Reynolds numbers considered in Sec. 4.2. The near-blade pressure distributions and flow patterns are compared in Sec. 4.3, and wake patterns of the model and full-scale propellers are compared in Sec. 4.4.

4.1. VALIDATION

4.1.1 Global forces

The open-water characteristics in non-cavitating conditions for the PPTC propeller are shown in Fig. 5, and for the TLP propeller in Fig. 6.

We produced the open-water curves for the PPTC from $J = 0.5 \dots 1.6$ and for the TLP from $J = 0.5 \dots 1.2$ with the SST $k-\omega$ turbulence model in model-scale (MS) conditions. Selected points are also simulated with the EARSM and $\gamma-Re_\theta$ models, as well as in full-scale (FS) conditions. The SST and EARSM simulations in model scale capture the propeller open water performance with good accuracy for both propellers. EARSM predicts slightly lower torque for the TLP propeller than the SST model. The transition simulations predict 2-3% higher thrust coefficient than the SST in model scale for the propellers, at the investigated points. The transition simulations, as well the full scale simulations, yield a slightly lower torque coefficient, and consequently, a little higher efficiency for the propeller.

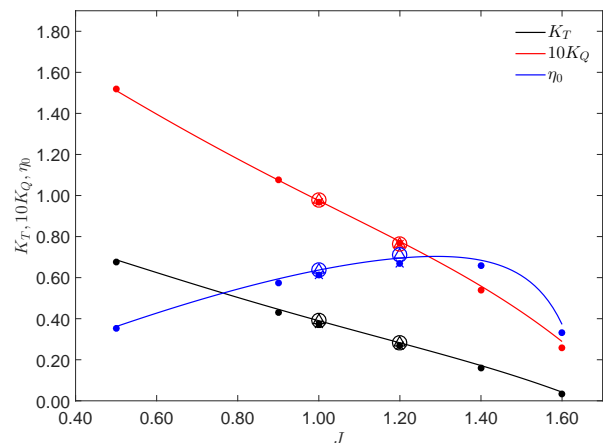


Figure 5: Open-water characteristics for the PPTC. Solid lines: experimental results; \bullet symbols denote corresponding $k-\omega$ model-scale simulations; \times symbols denote EARSM model-scale simulations; \triangle symbols denote $\gamma-Re_\theta$ model-scale simulations; \circ symbols denote $k-\omega$ full-scale simulations.

In the cavitating conditions for the PPTC, the thrust coefficient was determined in the experiments as $K_T = 0.374$. The model scale SST simulations in cavitating conditions predict $K_T = 0.369$ with 1% difference to the experimental value, the transition model predicts $K_T = 0.364$ with

3% difference, and the EARSM predicts $K_T = 0.367$ with 2% difference. The full scale SST simulations in cavitating conditions predict $K_T = 0.373$ with 0% difference to the experimental value.

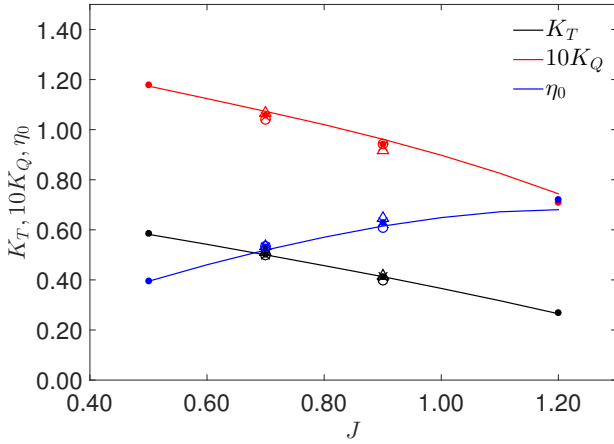


Figure 6: Open-water characteristics for the TLP. Solid lines: experimental results; \bullet symbols denote corresponding $k - \omega$ model-scale simulations; \times symbols denote EARSM model-scale simulations; \triangle symbols denote $\gamma - Re_\theta$ model-scale simulations; \circ symbols denote $k - \omega$ full-scale simulations.

In the cavitating conditions for the TLP, the thrust coefficient was determined in the experiments as $K_T = 0.493$. The model scale SST simulations in cavitating conditions predict $K_T = 0.503$ with 2% difference to the experimental value, the transition model predicts $K_T = 0.505$ with 2% difference, and the EARSM predicts $K_T = 0.501$ with 2% difference. The full scale SST simulations in cavitating conditions predict $K_T = 0.500$ with 1% difference to the experimental value.

4.1.2 Model-scale cavitation observation

The model-scale cavitation patterns of the PPTC propeller are compared in Figs. 7 and 8. The former figure shows the

cavitation type near the blades, and the latter figure shows the cavitation structures in the propeller slipstream. The experiments are compared to the results obtained with the different turbulence models. The propeller has strong tip vortex and hub vortex cavitation, which is visible in the experiments and in the simulations. The mean shape and extent of the root cavitation, as well as the tip and hub vortex cavitation, are captured well. The tip and hub vortex cavitation extending far behind the propeller is captured exceptionally well, as shown in Fig. 8. Also the modal shapes of the cavitating tip vortex are qualitatively well captured. Streak cavitation was observed in the experiments at several radial locations near the leading edge of the blade, while the simulation predicts sheet cavitation at the leading edge. The global cavitation is predicted similarly with each of the utilized turbulence models, although the transition model yields a bit narrower hub cavitating hub vortex.

The model-scale cavitation extent of the TLP propeller is compared in Fig. 9 for cavitation patterns near the blades, and in Fig. 10 for overall cavitation extent of the propeller. We show the experimental results together with those obtained with the different turbulence models. The propeller has sheet cavitation at around $0.9R$ which incepts at the leading edge. The simulations predict this, although the sheet starts at a slightly lower radius than in the experiments. The sheet cavitation covers almost the entire chord of the blade, and turns cloudy close to the trailing edge. No root cavitation is observed in the experiments or in the simulations. Bubble cavitation appears at the centre of chord at the top dead centre position. Upper part of the sheet cavity transforms into a cavitating tip vortex as it departs the blade. The cavitating tip vortex is relatively fine, and visible both in the experiments as well as in the simulations. As we see in Fig. 10, the cavitating tip vortex extends far in the propeller wake, and this behaviour is also captured well with the numerical simulations. Also the secondary fine tip vortex cavitation due to the end plate is captured in the CFD simulations, although it quickly diminishes after departing the blade. Again, the global cavitation is predicted similarly with each of the utilized turbulence models.

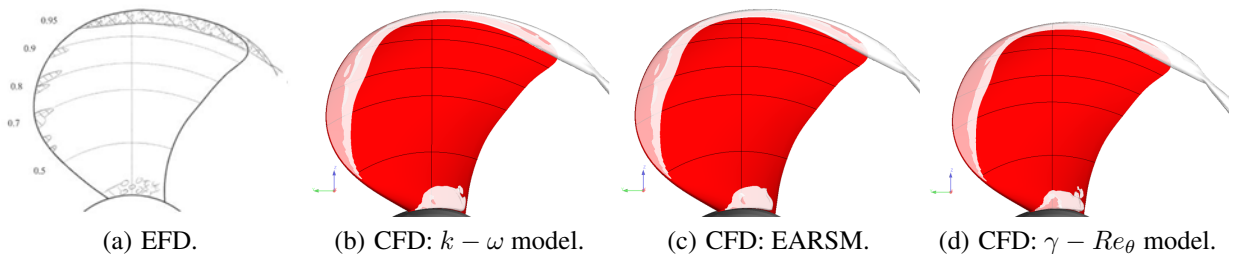


Figure 7: Comparison of near-blade cavitation patterns for the PPTC. The EFD result is given by Viitanen *et al.* (2017).

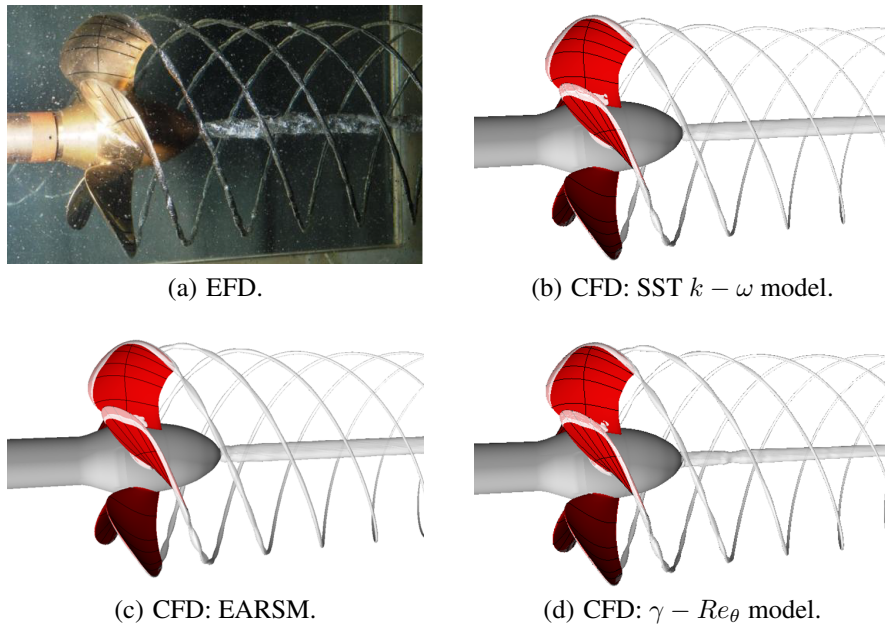


Figure 8: Comparison of model-scale cavitation patterns for the PPTC. The photograph from experiments is given by Heinke (2011).

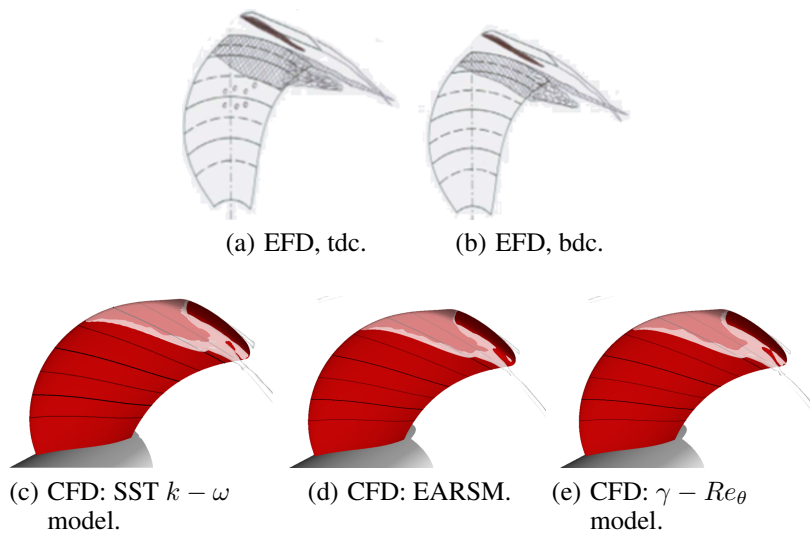


Figure 9: Comparison of near-blade cavitation patterns for the TLP. The top row shows the experimental cavitation sketches at top dead centre (tdc) and bottom dead centre (bdc).

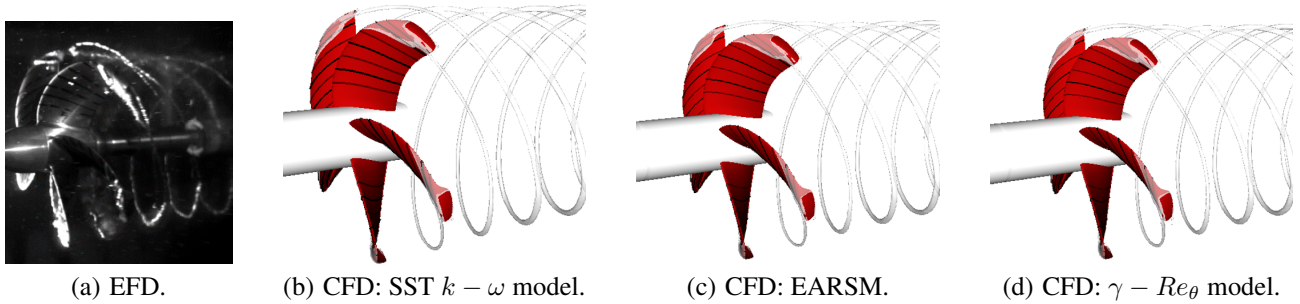


Figure 10: Comparison of model-scale cavitation patterns for the TLP.

4.1.3 A grid sensitivity study

Next, we carry out a grid sensitivity investigation for the PPTC propeller. We consider the model scale simulations at three different numerical grid densities. The fine grid simulations predict $K_T = 0.369$ with 1% difference to the experimental value, the medium grid simulations yield $K_T = 0.352$ with 6% difference, and the coarse grid sim-

ulations give $K_T = 0.343$ with 9% difference to the experiments. Fig. 11 displays the near-blade cavitation results and Fig. 12 shows the overall cavitation extent obtained with different numerical grid densities. Furthermore, we compare the pressure in the wake in Fig. 13 with the three grids. We evaluated the pressure coefficient, $C_p = 2(p - p_\infty)/(\rho_\infty n^2 D^2)$, in the wake at the track of the tip vortex, similarly as is done in Fig. 20(a) in Sec. 4.4.

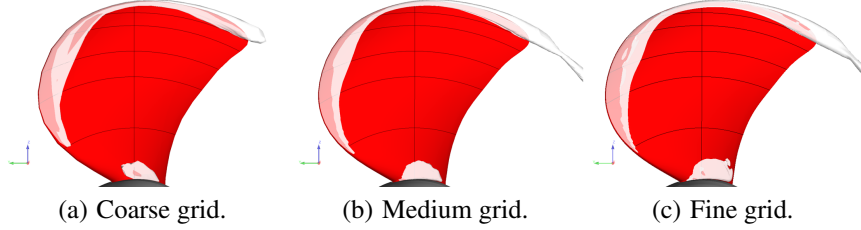


Figure 11: Comparison of near-blade cavitation results with different grid densities. Model-scale simulations.

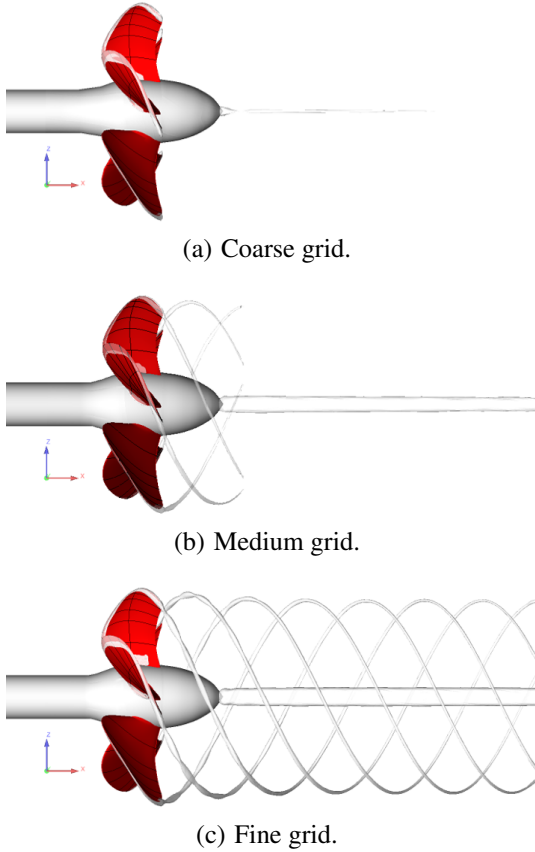


Figure 12: Comparison of cavitation patterns for the PPTC propeller with different grid densities. Model scale simulations.

The cavitation near the propeller blades is similar with the different utilized grids. All grids predict sheet cavitation at the leading edge, which then transforms to the tip vortex cavitation. The root cavitation grows in extent as the grid is refined, but otherwise the near-blade cavitation is simi-

lar between the different grid densities. We observe greater differences in the results between the different grids in the propeller wake. The coarse grid simulations yield a very limited vortex cavitation, as the tip vortex cavitation seizes just after the blade trailing edge, and the hub vortex cavitation being fine and limited in length. The medium grid simulations give the hub vortex cavitation that match better the fine grid results, and the experiments, but the tip vortex cavitation extends less than one diameter in the axial direction. The modal shapes are also absent in the medium grid solution. Fig. 13 shows the dissipation in the pressure is notably greater for the coarse and medium grids as the axial distance from the propeller increases. The pressure coefficient in the first vortex core for the coarse grid is significantly less than the vapour pressure, and hence the tip vortex cavitation terminates just after the blades. For the medium grid, the first tip vortex core on the curve maintains a low C_p level, and we observed a cavitating vortex in Fig. 12(b). Beyond this, dissipation decreases the pressure coefficient, and the tip vortex cavitation disappears.

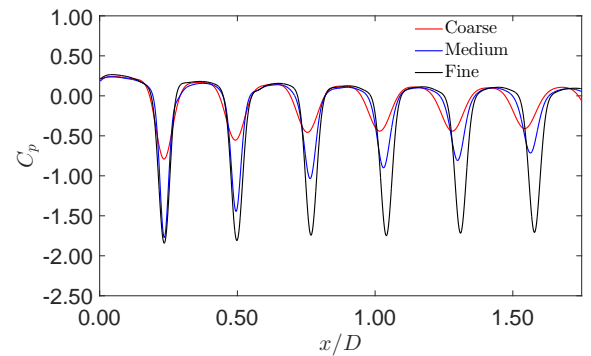


Figure 13: Pressure coefficient in the track of the tip vortex with different grid densities for the PPTC propeller.

4.2. MODEL- AND FULL-SCALE CAVITATION PATTERNS

Next, we compare the cavitation patterns in model and full scale for the PPTC. Cavitation close to the blades and the overall cavitation patterns are visualized in Fig. 14. In both cases, the results with the SST model are shown. Cavitation patterns are very similar between the different simulations. The tip and hub vortex shape and extent were well reproduced also in full-scale conditions, although the extent of the tip vortex cavitation is slightly less in the full scale. The root cavitation area appears as larger in the full-scale conditions, extending past the trailing edge of the blades.

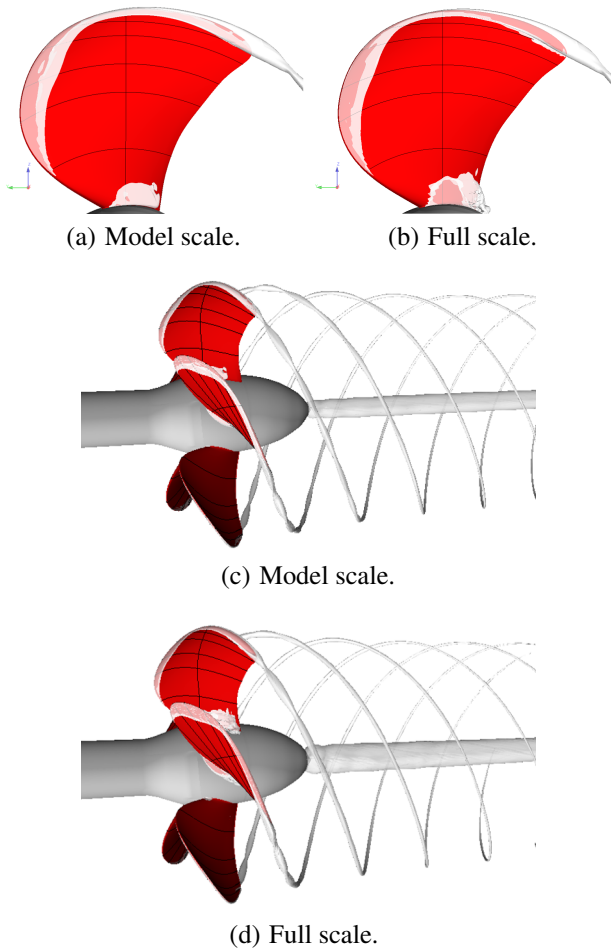


Figure 14: Comparison of the predicted cavitation patterns for the PPTC in model- and full-scale conditions. Both results are from SST $k - \omega$ simulations. The black circles on the blades show the reference radii.

We compare the cavitation patterns of the TLP propeller in the model- and full-scale conditions. Fig. 15 shows the cavitation close to the blades and the overall cavitation patterns. The results obtained with the SST model are shown. The cavitation patterns on the blades mostly resemble each other in model- and full-scale conditions. The tip vortex shape and extent in the full-scale conditions were similar to the model scale observations, although the extent of the

tip vortex cavitation was less in the full scale. The model-scale cavitation detaches from the blade before the trailing edge, and the sheet cavitation covers the entire blade surface in full scale. In the full scale conditions, this cavity detachment is different, as it remains attached to the blade until the trailing edge. The sheet cavitation transforms into vortex cavitation before the tip of the blade in both cases. Cavitation of the secondary tip vortex due to the endplate is visible in both simulations, although the very fine vortex cavitation does not extend very far in either case.

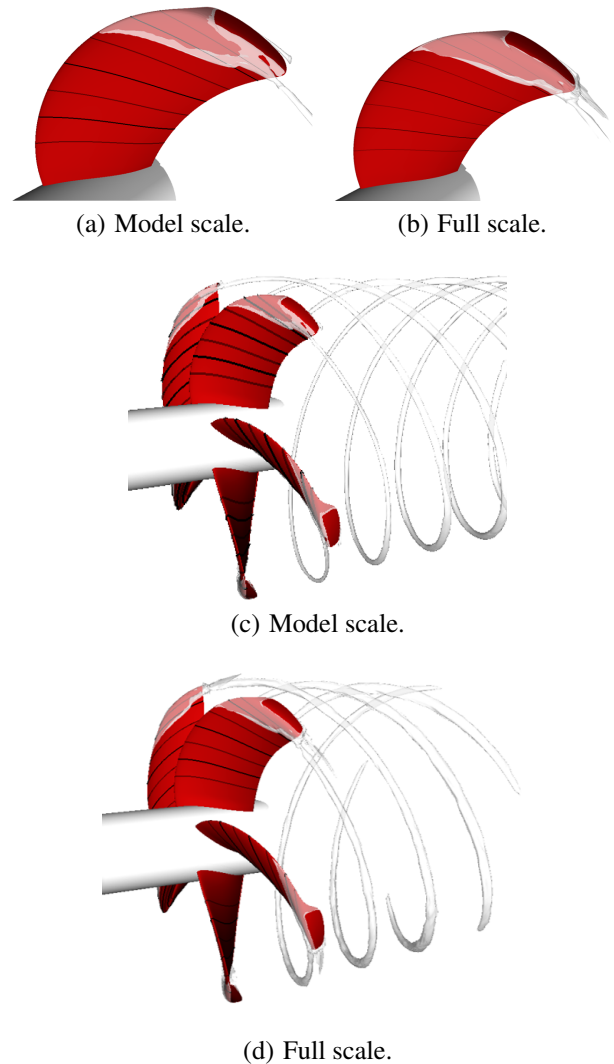


Figure 15: Comparison of the predicted cavitation patterns for the TLP in model- and full-scale conditions. Both results are from SST $k - \omega$ simulations. The black circles on the blades show the reference radii.

Next, we investigate the rate of evaporation within the cavity volume in Fig. 16 for the PPTC propeller. Here, the rate of evaporation is visualized at various cuts in the cavity volume in the axial direction. Also the surface-restricted streamlines on the blades are shown. The figure shows both the model- and full-scale results for the propeller, and the model-scale results are those obtained with the SST and the

transition models. The boundary layer flow is further discussed in Sec. 4.3. The rate of evaporation in model scale is strong at the core of the tip vortex, whereas condensation occurs at the outer edge of the cavitating vortex. Similar trends are also present in the full scale, although the rate is less. A more complex interplay of the evaporation and condensation takes place on the sheet cavities close to the blades. The sheet cavity closure line near the leading edge, and corresponding transition between the evaporation and condensation, shifts toward a greater chord length from the leading edge in full-scale conditions. This is evidenced also by the orientation of the blade surface flow, where the streamlines on the surface are more straight in the full-scale until the location of the re-entrant jet. The flow within the sheet cavitation near the leading edge is more complex in model scale. The model scale simulations with the SST and transition model yield relatively similar results.

We investigate the rate of evaporation within the cavity volume for the TLP propeller in Fig. 17. Similarly as above, the rate of evaporation is visualized at various cuts in the cavity volume in the axial direction. Also the surface-

restricted streamlines on the blades are shown. The figure shows both the model- and full-scale results for the propeller, and the model-scale results are those obtained with the SST and the transition models. The boundary layer flow is further discussed in Sec. 4.3.

The rate of evaporation in model scale is stronger for the TLP at the core of the tip vortex, when compared to the PPTC case. The TLP propeller has a little lower J value, and the cavitating tip vortex is finer. Condensation occurs at the outer edge of the cavitating vortex. These trends are also present in the full scale, and again the rate of evaporation is less. The sheet cavity on the blade surface is quite thick. Evaporation seems to dominate closer to the leading edge, whereas more condensation is seen closer to the mid-chord position. The surface-restricted streamlines are more straight in full scale, also underneath the sheet cavity. The flow within the sheet cavitation is more complex in the model scale, which is visible in both the SST and transition simulations. The model scale simulations with the SST and transition model yield, again, similar results.

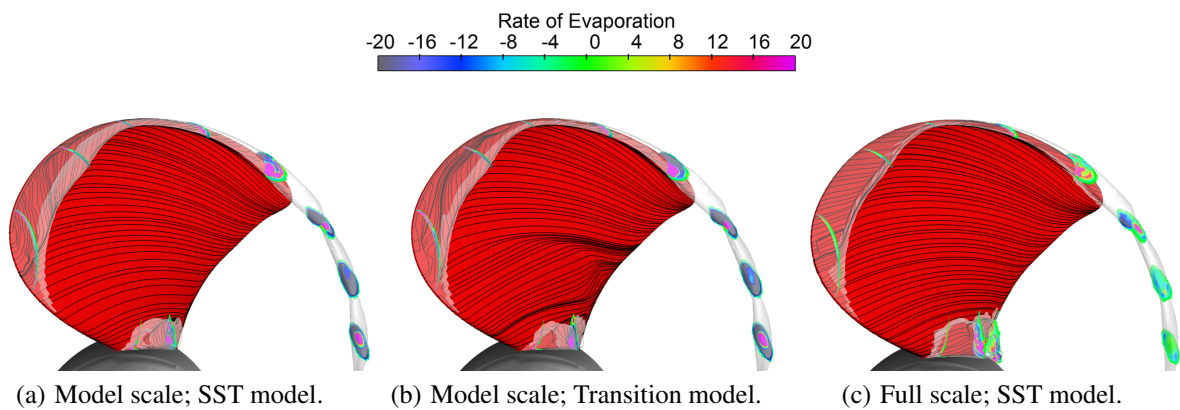


Figure 16: Rate of evaporation (in $[\text{kg}/\text{m}^3\text{s}]$) within the cavity volume in model and full scale for the PPTC propeller. Perspective views near one blade. Cavitation is shown as the grey transparent surface, and the surface-restricted streamlines on the blades as the black curves.

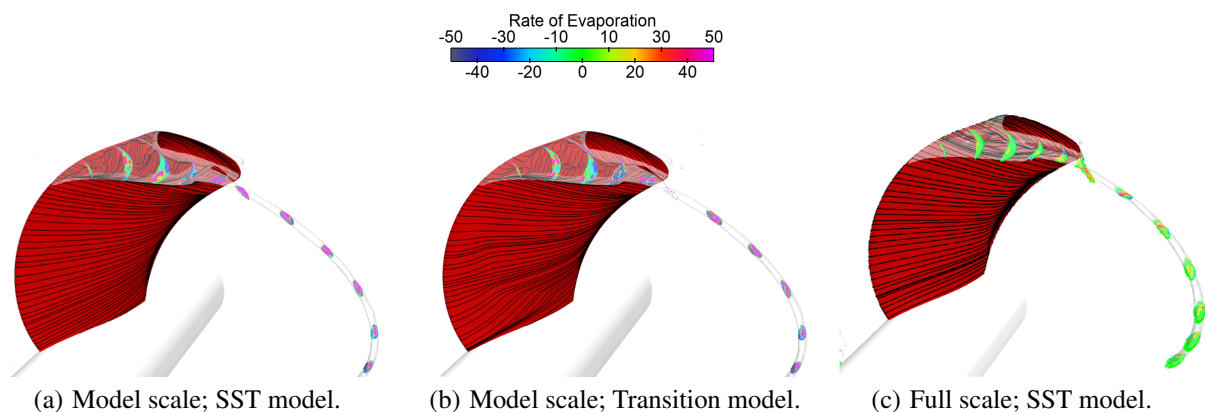


Figure 17: Rate of evaporation (in $[\text{kg}/\text{m}^3\text{s}]$) within the cavity volume in model and full scale for the TLP propeller. Perspective views near one blade. Cavitation is shown as the grey transparent surface, and the surface-restricted streamlines on the blades as the black curves.

4.3. NEAR-BLADE FLOW AND PRESSURE DISTRIBUTIONS IN MODEL- AND FULL-SCALE

The surface-restricted streamlines, together with the pressure coefficient are shown on the PPTC propeller blade in Fig. 18. Here, we compare the model-scale SST and $\gamma-Re_\theta$ transition model simulations, and the full-scale SST simulations. For reference, the same radii as before are shown as the black circles drawn on the blades. The pressure distributions are similar in the model scale SST and transition simulations. A slightly lower pressure is seen at the middle of the blade in full scale. Also, a higher surface pressure in the tip area, below the cavitation zone, is seen for the full scale conditions. The boundary layer flow was mostly circumferentially directed along the blade for the model and full scale SST simulations. In fact, the SST model predicts fully turbulent flow also in the model scale, and little difference in the surface streamlines is seen between the two SST simulations.

A clear difference in the surface streamlines for the PPTC in Figs. 16 and 18 is seen in the areas covered by the sheet cavitation. The model scale simulations using the SST and transition models show a main flow direction under the sheet cavity before the cavity closure line that is more wavy and radially directed, whereas the surface streamlines are more organized and circumferentially oriented in full scale. The transition model predicts a laminar flow region below $0.7R$, as sketched by the dashed black curve in Fig. 18(b). The effect of cavitation on the surface restricted stream-

lines is significant. The re-entrant jets in both model and full scale simulations are directed towards the cavitating tip vortex at the closure line of the sheet cavitation as observed before in model scale conditions (Sipilä, 2012; Viitanen & Siikonen, 2017). The location of the cavity closure line and corresponding increase in the surface pressure are similar in the model and full scale simulations.

The surface-restricted streamlines and the pressure coefficient are shown on the TLP propeller blade in Fig. 19. We compare the model-scale SST and transition model simulations, and the full-scale SST simulations. The same reference radii as before are shown as the black circles drawn on the blades. The pressure distributions are mainly very similar between the model scale and full scale simulation. The pressure is slightly less in full scale near the detachment of the sheet cavity, and then grows to larger values near the trailing edge.

Also for the TLP propeller, a clear difference in the surface streamlines is seen in the areas covered by the sheet cavitation in Figs. 17 and 19. The flow underneath the sheet cavity is more regular and circumferentially oriented in full scale than in the model scale conditions, although this has little effect in the pressure distributions which are limited by the vapour pressure. The SST model again predicts fully turbulent flow also in the model scale, and little difference in the surface streamlines is seen between the two SST simulations, except for the area covered by the sheet cavitation. The transition model predicts a laminar flow region below $0.5R$, and this is sketched by the dashed black curve.

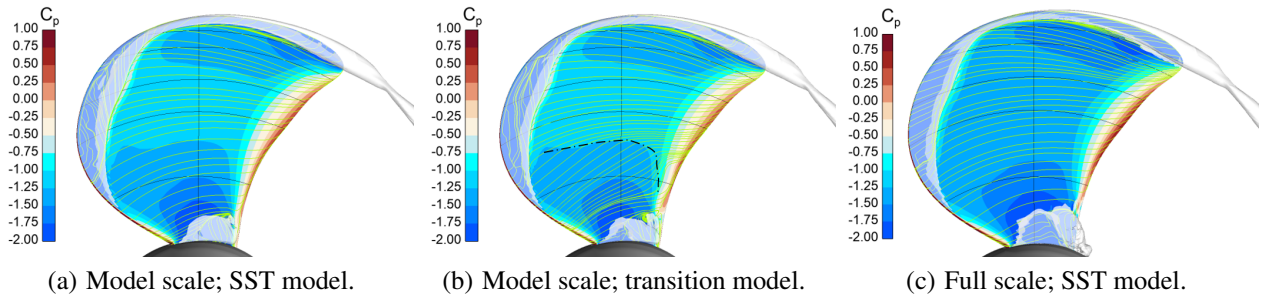


Figure 18: Surface-restricted streamlines (in green) and the surface pressure distributions for the PPTC propeller. Cavitation is shown as the grey transparent surface.

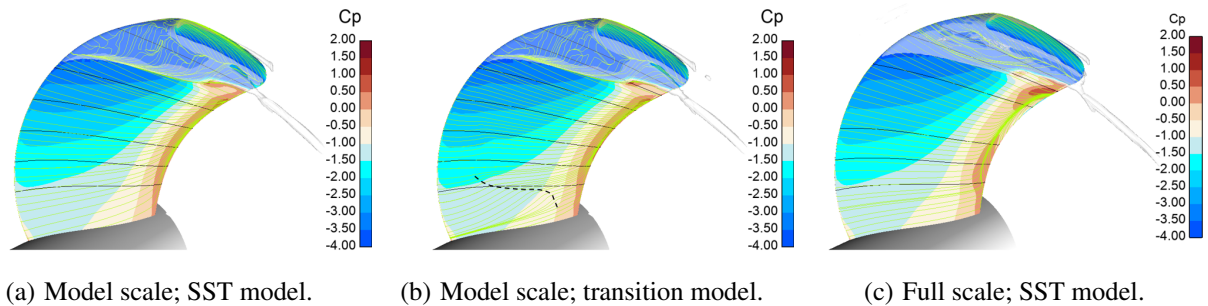


Figure 19: Surface-restricted streamlines (in green) and the surface pressure distributions for the TLP propeller. Cavitation is shown as the grey transparent surface.

4.4. PROPELLER WAKE FLOW CHARACTERISTICS IN MODEL AND FULL SCALE

The pressure coefficient in the PPTC propeller wake is visualized in Fig. 20. The figure shows the model scale SST and transition simulations, together with the full scale SST simulations. The black dashed curve in Fig. 20(a) denotes the track of the tip vortex on the x, z -plane; we evaluate the pressure coefficient and the eddy viscosity ratio on that line as a function of the axial distance in Fig. 22. The eddy viscosity is visualized in Fig. 21 within the cavity volume for the propeller, where the eddy viscosity ratio is shown at various cuts in the cavity volume in the axial direction. Also the surface-restricted streamlines on the blades are shown.

As we see in the pressure coefficients, a strong tip vortex is preserved well in the slipstream. The pressure is limited by the vapour pressure in the tip and hub vortices. The local wakes that have detached from the blades are visible in the C_p values, being more distinct in the model scale, especially with the transition model. The transition model predicts more variation in the slipstream pressure.

The pressure distributions in the wake are similar with the model and full scale SST simulations. Then again, the pressure in the tip vortex shows more dissipation in the full scale simulations than in the model scale simulations. The pressure maintains a low value throughout the wake in the tip vortex core with the transition model simulations. The eddy viscosity within the tip vortex core drops to zero, and grows in magnitude with the radius of the vortex. Notable secondary peaks in μ_t/μ values in Fig. 22(b) are visible behind the tip vortex in all cases, although these peaks drop rapidly in magnitude. The eddy viscosity inside the tip vortex core and in its vicinity increases with the axial distance with the SST model in model scale, whereas it stays low with the transition model. The eddy viscosity remains low in the full scale conditions.

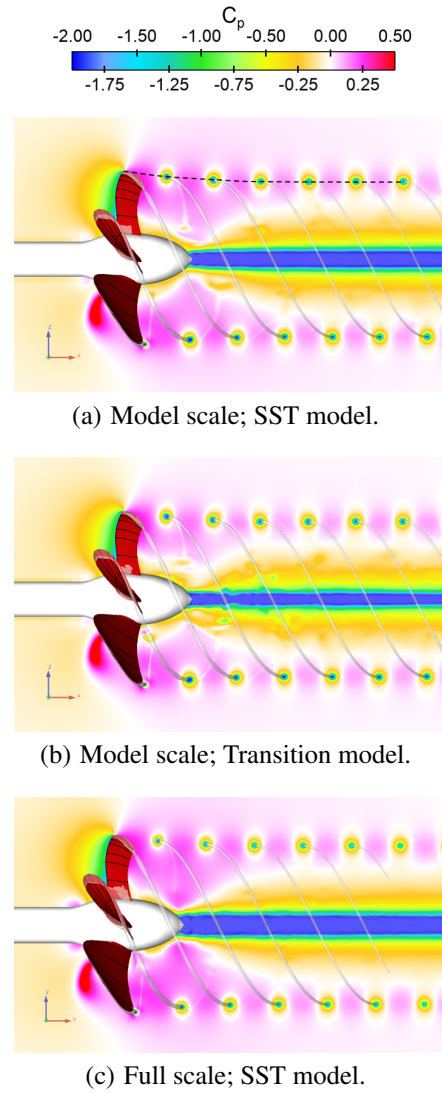


Figure 20: Pressure coefficient in the PPTC propeller wake in model and full scale.

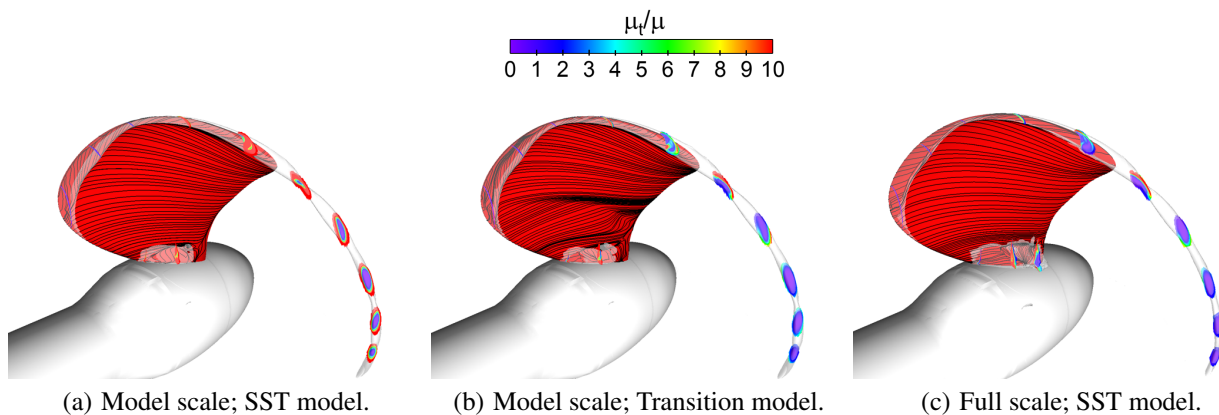
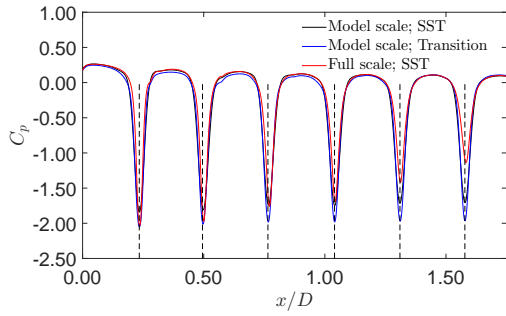
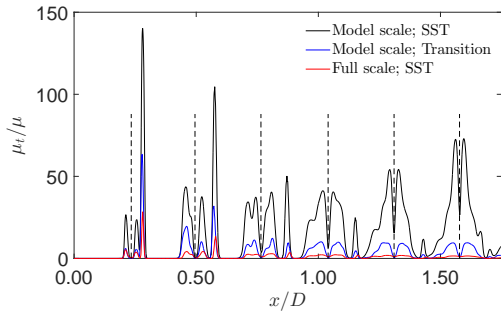


Figure 21: Eddy viscosity within the cavity volume in model and full scale. Perspective views near one blade. Cavitation is shown as the grey transparent surface, and the surface-restricted streamlines on the blades as the black curves.

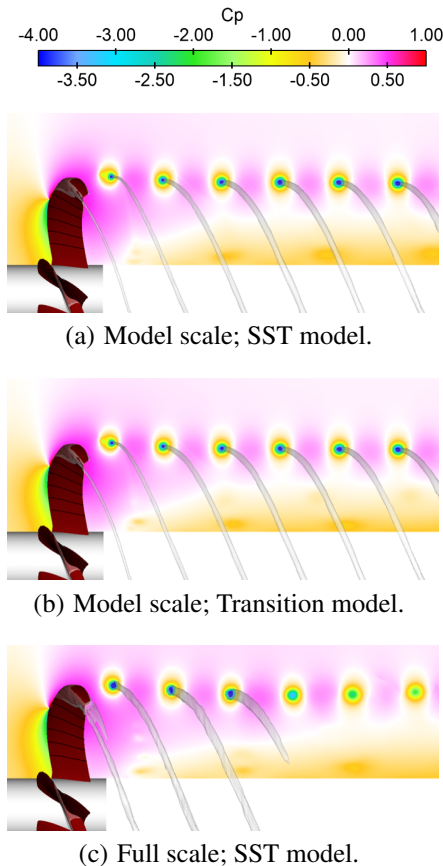


(a) Pressure coefficient.



(b) Eddy viscosity.

Figure 22: Pressure coefficient and eddy viscosity in the track of the tip vortex in model and full scale for the PPTC propeller. The values are evaluated on the curve shown in Fig. 20. The black dashed vertical lines denote the locations of the tip vortex cores.



(a) Model scale; SST model.

(b) Model scale; Transition model.

(c) Full scale; SST model.

Figure 23: Pressure coefficient in the TLP propeller wake in model and full scale.

The pressure coefficient in the TLP propeller wake is visualized in Fig. 23. The figure shows the model scale SST and transition simulations, together with the full scale SST simulations. We note more dissipation in the full scale simulations, and the tip vortex cavitation vanishes sooner in the full scale conditions. The pressure inside the remaining tip vortex cores has a lower negative value in the full scale. Albeit more dissipation is seen in the full scale conditions, the tip vortex appears as thicker as in the model scale. The local wakes in the slipstream behind the blades are better visible in the model scale. The model scale simulations show the secondary vorticity created by the endplate at the location of the first tip vortex pressure peak. This, however, disappears quite soon, and it is no more visible at farther distances from the propeller. In the model scale, the cavitating tip vortex grows in thickness as the axial distance increases. We note a similar tendency in the full scale simulations. It also appears that in full scale, the wake contraction changes and it actually gets wider after the fourth tip vortex on this plane. Overall, less difference is seen in the model scale SST and transition simulations than with the PPTC propeller case.

5. DISCUSSION

We have numerically investigated single and two-phase flows around marine propellers in open-water conditions at different Reynolds number regimes. Two types of marine propellers were considered: a conventional and a tip-loaded one. The simulations were carried out using a homogeneous two-phase flow model with RANS turbulence modelling approaches. Transition was accounted for in model scale simulations by employing a LCTM transition model. In the model scale, also an anisotropic RANS model was utilized.

A grid refinement study was conducted in model scale. All grids predicted the near-blade cavitation patterns rather similarly, and greater differences were seen in the wake where numerical dissipation due to a coarser grid affects the slipstream characteristics and the vortex cavitation patterns. We observed similar results in the full-scale simulations with coarse, medium and fine grids, although these were not shown here.

The model-scale propeller performance and cavitation patterns are captured well in the numerical simulations, with little difference between the utilized turbulence models in the model-scale conditions. A tendency of increased cavitation extent is observed as the Reynolds number increases. The hub vortex for the PPTC propeller was clearly thicker in the full-scale simulation, and also thicker in the model-scale SST case (fully turbulent) than in the transition model simulation. Similarly, root cavitation was larger in full-scale. The same trend was observed in the tip vortex cavitation for the TLP propeller for which the loading was higher: the thickness of vortex cavitation was larger in full-scale than in model-scale. At the same time, dissipation of the

cavitating tip vortex was also greater in the full-scale conditions which was seen especially with the TLP.

Mainly sheet and vortex cavitation were predicted by the model- and full-scale simulations. Closer inspection revealed clear differences in wake flow characteristics, and in phase change phenomena within the cavitation. In the present investigations, we observed that water evaporated at a lower rate in the full-scale tip vortex core, and that the eddy viscosity was quite low in the cavity at full scale.

A clear difference in the surface streamlines between the model- and full-scale simulations was seen in the areas covered by the sheet cavitation for both investigated propellers. The near-blade flow underneath the sheet cavity was more regular and circumferentially oriented in full-scale than in the model-scale conditions.

The model-scale results can, however, be sensitive to the utilized turbulence model especially with respect to the wake flow characteristics, as has been observed before (Guilmineau *et al.*, 2015; Sipilä *et al.*, 2014; Viitanen & Siikonen, 2017). An investigation using different turbulence models should be carried out in full scale. Unsteady RANS and higher fidelity turbulence modelling approaches are planned in the future for the full-scale cavitating propeller. Additionally, the sensitivity of the transition model to the initial turbulence field quantities in the model-scale performance predictions for the cavitating propellers needs to be assessed.

ACKNOWLEDGEMENTS

The authors are very grateful to Mr. Michael Brown from NSWCCD for providing the experimental results of the TLP propeller in the forms of open-water data and cavitation tunnel results.

REFERENCES

- Amromin, E. 2015. Estimations of scale effects on blade cavitation. *In: Journal of Physics: Conference Series*, vol. 656. IOP Publishing.
- Baltazar, J., Rijpkema, D., & Falcão de Campos, J. 2018. On the use of the γ - Re_θ transition model for the prediction of the propeller performance at model-scale. *Ocean Engineering*, **170**, 6–19.
- Choi, Y. H., & Merkle, C. L. 1993. The application of preconditioning in viscous flows. *Journal of Computational Physics*, **105**, 207–230.
- Dong, X.-Q., Li, W., Yang, C.-J., & Noblesse, F. 2018. RANSE-based Simulation and Analysis of Scale Effects on Open-Water Performance of the PPTC-II Benchmark Propeller. *Journal of Ocean Engineering and Science*.
- Guilmineau, E., Deng, G.B., Leroyer, A., Queutey, P., Vissonneau, M., & Wackers, J. 2015. Influence of the Turbulence Closures for the Wake Prediction of a Marine Propeller. *In: Fourth International Symposium on Marine Propulsors (smp'15)*.
- Heinke, H. J. 2011. Potsdam Propeller Test Case (PPTC). Cavitation Tests with the Model Propeller VP1304. *SVA Potsdam Model Basin Report No.3753*.
- Hellsten, A. 2002. Curvature corrections for algebraic Reynolds stress modeling: a discussion. *AIAA Journal*, **40**(9), 1909–1911.
- Hellsten, A., Wallin, S., & Laine, S. 2002. Scrutinizing curvature corrections for algebraic Reynolds stress models. *In: 32nd AIAA Fluid Dynamics Conference*. AIAA. AIAA paper 2002–2963.
- Langtry, R. B. 2006 (May). *A Correlation-Based Transition Model using Local Variables for Unstructured Parallelized CFD codes*. Ph.D. thesis, University of Stuttgart, Stuttgart, Germany.
- Langtry, R.B., Menter, F.R., Likki, S.R., Suzen, Y.B., Huang, P.G., & Völker, S. 2006. A correlation-based transition model using local variables Part II: Test cases and industrial applications. *Journal of Turbomachinery*, **128**(3), 423–434.
- Menter, F.R. 1992. Influence of freestream values on $k - \omega$ turbulence model predictions. *AIAA Journal*, **30**(6), 1657–1659.
- Menter, F.R., Langtry, R.B., Likki, S.R., Suzen, Y.B., Huang, P.G., & Völker, S. 2006. A correlation-based transition model using local variables Part I: model formulation. *Journal of turbomachinery*, **128**(3), 413–422.
- Miettinen, A., & Siikonen, T. 2015. Application of pressure- and density-based methods for different flow speeds. *International Journal for Numerical Methods in Fluids*, **79**(5), 243–267. doi:10.1002/flid.4051.
- Müller, S.-B., Abdel-Maksoud, M., & Hilbert, G. 2009. Scale effects on propellers for large container vessels. *In: First International Symposium on Marine Propulsors*.
- Rijpkema, D., Baltazar, J., & Falcão de Campos, J. 2015. Viscous flow simulations of propellers in different Reynolds number regimes. *In: Proceedings of Fourth International Symposium on Marine Propulsors, Austin, Texas*.
- Roe, P. L. 1985. Some contributions to the modelling of discontinuous flows. *Pages 163–193 of: Large-scale computations in fluid mechanics*.
- Sánchez-Caja, A, González-Adalid, J, Pérez-Sobrino, M, & Sipilä, Tuomas. 2014. Scale effects on tip loaded propeller performance using a RANSE solver. *Ocean Engineering*, **88**, 607–617.
- Sipilä, T. 2012 (September). *RANS analyses of cavitating propeller flows*. Licentiate Thesis, Aalto University, School of Engineering.

- Sipilä, T., Sánchez-Caja, A., & Siikonen, T. 2014 (July). Eddy vorticity in cavitating tip vortices modelled by different turbulence models using the RANS approach. *In: 6th European Conference on Computational Fluid Dynamics, (ECFD VI)*.
- Van Leer, B. 1982. Flux-Vector Splitting for the Euler Equations. *In: Proceedings of the 8th International Conference on Numerical Methods in Fluid Dynamics*. (also Lecture Notes in Physics, Vol. 170, 1982).
- Viitanen, V., Hynninen, A., Lübke, L., Klose, R., Tanttari, J., Sipilä, T., & Siikonen, T. 2017 (June 1 – 3). CFD and CHA simulation of underwater noise induced by a marine propeller in two-phase flows. *In: Fifth International Symposium on Marine Propulsors (smp'17)*.
- Viitanen, V. M., & Siikonen, T. 2017 (May 11 – 12). Numerical simulation of cavitating marine propeller flows. *In: 9th National Conference on Computational Mechanics (MekIT17)*. International Center for Numerical Methods in Engineering (CIMNE), pp. 385–409. Trondheim, Norway. ISBN: 978-84-947311-1-2.
- Viitanen, V. M., Hynninen, A., Sipilä, T., & Siikonen, T. 2018. DDES of Wetted and Cavitating Marine Propeller for CHA Underwater Noise Assessment. *Journal of Marine Science and Engineering*, **6**(2), 56.
- Wallin, S., & Johansson, A. 2001 (June). Modelling of streamline curvature effects on turbulence in explicit algebraic Reynolds stress turbulence models. *In: Second International Symposium on Turbulence and Shear Flow Phenomena*.